Journal of the Korean Physical Society
https://doi.org/10.1007/s40042-021-00342-5

Online ISSN 1976-8524
Print ISSN 0374-4884

ORIGINAL PAPER - ATOMS, MOLECULES AND OPTICS

Long-range distribution of high-quality time-bin entangled photons for quantum communication

Jin-Hun Kim[1] · Jin-Woo Chae[1] · Youn-Chang Jeong[2] · Yoon-Ho Kim[1]

Received: 9 September 2021 / Revised: 8 October 2021 / Accepted: 25 October 2021

Abstract

Entanglement is an essential ingredient in current experimental implementations for quantum communication. Nevertheless, distributing the entangled states to distant users, in high quality, via widely installed fiber channels has been a daunting problem. Here, we report an experimental distribution of high-quality entangled qubits over long-distance fiber channels, especially by using time-bin mode due to its outstanding robustness in fiber-optic distributions. In particular, by employing actively operating feedback schemes, we clearly demonstrate that the time-bin entanglement can be reliably shared between two distant parties, each separated by up to 60 km in all fiber-based implementations; then, we prove the significance of our study in long-range, long-lasting quantum communication by showing a high value of two-photon interference visibilities and a violation of the Clauser–Horne–Shimony–Holt Bell inequality.

Keywords Quantum communication · Quantum network · Fiber optics communication

1 Introduction

Quantum entanglement has become an important resource in quantum communication (QC) to enable implementation of specific entanglement-based communication tasks that are not possible classically, such as, quantum key distribution (QKD) [1–3], quantum teleportation [4–7], and quantum secret sharing [8–10]. Such entanglement cannot be created by just local operations and classical communication at distant sites; rather, it should be prepared in advance and distributed directly to users for the quantum communication tasks. Photons have been regarded as the best entanglement carrier for long-distance applications due to their capability to be transported in fiber-optic channels. Indeed, photons can carry in-depth information through fiber channels at a high speed and with low transmission loss [11–14], and the use of photons can allow us to use the worldwide implemented optical fiber network [15, 16]. Given the importance of entanglement distribution in fiber-based implementations, many technical demonstrations have been experimentally realized via optical fiber links [17–22], and these developments certainly constitute essential building blocks toward the global fiber quantum network.

For the practical deployment of quantum communication tasks, however, there remain unresolved technical problems for distributing entanglement primarily via fiber channels, and one crucial issue yet to be solved is that the entangled qubit must be robust against any decoherence in optical fibers to enable quantum communication tasks in long-distance fiber channels. Thus, the more pertinent way to encode qubits could be time-bin encoding, i.e., a discrete version of energy-time entanglement [23–27]. Compared with polarization encoding, which is well-known for its easy free-space manipulation based on simple linear optics, time-bin qubits are more robust for long-distance applications because they are inherently invulnerable against polarization mode dispersion and drifts in optical fibers, and their chromatic dispersion effects can also be passively compensated for by using linear optics [28]. Indeed, such encoding type is proven to be well suited for transmission over more than 100 km of optical fiber [27, 29] and has already been exploited for quantum cryptographic protocols [30, 31].

✉ Jin-Hun Kim
kimjinhun1124@gmail.com

✉ Yoon-Ho Kim
yoonho72@gmail.com

1 Department of Physics, Pohang University of Science and Technology (POSTECH), Pohang 37673, Korea

2 The affiliated Institute of ETRI, Daejeon 34044, Korea

Published online: 15 December 2021

Here, we report a quantum communication system capable of distributing high-quality entangled qubits reliably over long-distance fiber channels, effectively employing the time-bin degree of freedom. In actuality, significant complexities remain for time-bin entangled qubits in the way of encoding phase information, particularly in the fiber-based environment; correct phase encoding relies on the most stable interferometers to address a thermally induced phase decoherence. While time-bin entanglement has been a subject of recent interest, previous attempts, due to their simplicity, have mostly been focused on just temperature control in the phase change of interferometers [23, 24, 27]. If interferometers are to achieve operation stability, they need to be actively stabilized. Here, we develop an actively operating feedback scheme that consists of probing the interferometer's phase with a frequency stabilized auxiliary CW laser and locking them to a desired phase via an actively-driven feedback loop. With the qualified stabilization system, we demonstrate that high-quality time-bin entanglement can be distributed between distant users reliably in all fiber-based implementations, which clearly proves the significance of our study in the field of the fiber-optically networked entanglement-based quantum communication.

2 Experimental section and Method

The experimental setup for distributing time-bin entangled photons toward two users, i.e., Alice and Bob, is represented in Fig. 1. The overall scheme consists of the source of entangled time-bin photon pairs, the distribution quantum channels based on the dense wavelength-division multiplexing (DWDM) filters, the length of which is implemented by the use of fiber-optic spools, and the analysis stage of distributed time-bin qubit pairs performed by Alice and Bob.

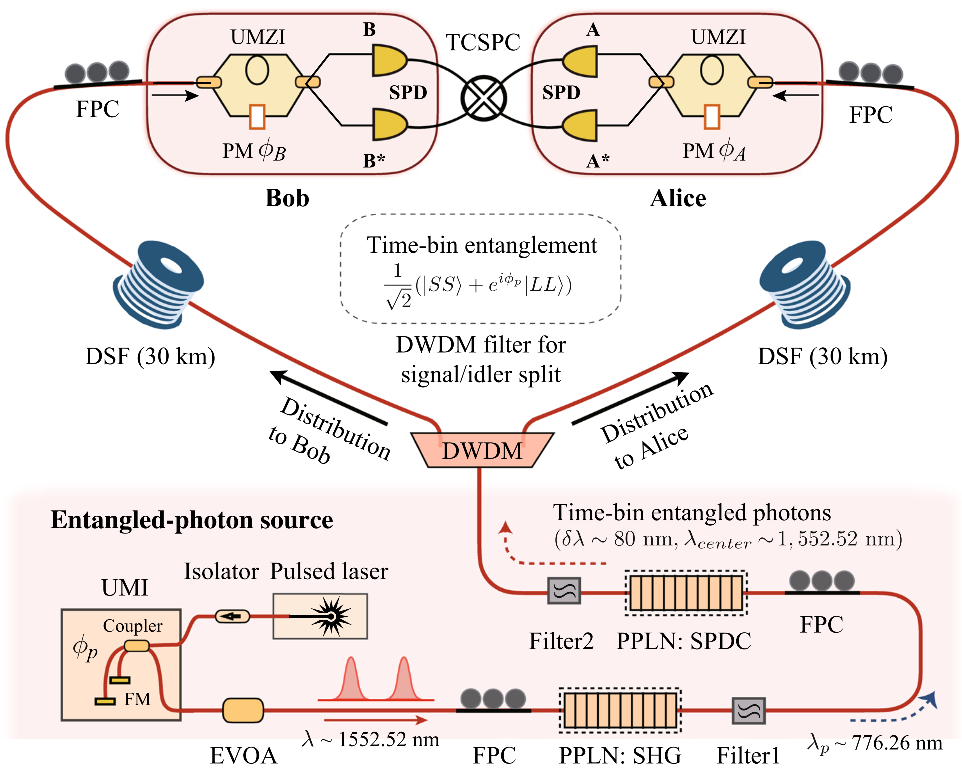

Fig. 1 Schematic optical setup for a high-quality time-bin entanglement distribution in all fiber-based implementations. Time-bin photonic modes are prepared by passing a laser pulse (Ch. 31, λ = 1,552.52 nm) through the UMI, and eventually, the second harmonic of the coherent double pulses from a PPLN: SHG crystal, i.e., pump (λ_p = 776.26 nm), produces broadband time-bin entangled photons ($\delta\lambda \sim 80$ nm, $\lambda_{center} \sim 1552.52$ nm) via the type-0 SPDC process in a PPLN crystal. Separated from the DWDM components (i.e., λ_s=1549.32 nm, λ_i=1555.75 nm, and $\delta\lambda_{s,i}$=1.2 nm), signal and idler photons are distributed to Alice and Bob, respectively, through a 30-km channel of optical fibers. Then, Alice and Bob analyze the time-bin entangled photons on phases ϕ_A and ϕ_B by using UMZIs equally unbalanced with respect to the UMI. All interferometers (an UMI and two UMZIs) are actively stabilized using a well-organized feedback system for a reliable quantum communication. *DWDM* dense wavelength-division multiplexing, *UMI* unbalanced Michelson interferometer, *FM* faraday mirror, *EVOA* electronic variable optical attenuator, *FPC* fiber polarization controller, *PPLN* periodically-poled lithium niobite, *SHG* second harmonic generation, *SPDC* spontaneous parametric down-conversion, *UMZI* unbalanced Mach-Zehnder interferometer, *PM* phase modulator. *DSF* dispersion-shifted fiber

In the following, we describe in detail the overall experimental setup, i.e., how it is organized optically and electronically, and we present how well the overall QC system works with the associated experimental results. See Sect. 2.1 for entanglement source and Sect. 2.2 for entanglement analysis setup. We then analytically explain how to verify entanglement and how to characterize our QC system in terms of two-photon visibility. Finally, we present the experimental results of distributing time-bin entanglement given the experimental setup, thereby showing the importance of our study for fiber-implemented entanglement-based quantum communication.

2.1 Time-bin entangled-photon source

Here, we describe the source of entangled time-bin photon pairs (For detailed structure, see the Fig. 2). A time-bin qubit is formed by a coherent superposition of photonic quantum states in two separate temporal modes. For the state preparation, a mode-locked picosecond fiber laser (Calmar Laser, FPL-02CTT) operating at a repetition rate of 18.02 MHz and at a wavelength of 1,552.52 nm (DWDM Ch. 31 in ITU grid) is exploited, and its wavelength is frequency-doubled, as a pump light, to 776.26 nm from the the second harmonic generation (SHG) module, which includes a bulk type-0 PPLN crystal (polling period of 19.3 μm and crystal length of 35 mm; HC Photonics). The residual telecomband radiations are suppressed by following Filter 1 up to 80 dB while allowing for pump transmission (with 2.0-dB insertion loss). Before the SHG module, the laser pulse passes through an unbalanced Michelson interferometer (UMI), as shown in Fig. 2b, to produce a pair of coherent pulses, defining the two-dimensional time bin modes with a relative phase ϕ_p between the two arms (temporal separation $\Delta\tau_p \sim 3.6$ ns).

Then, the twin pump pulses (with a relative phase ϕ_p) create the time-bin two-photon state with spectral correlation via a spontaneous parametric down-conversion (SPDC) process at the type-0 waveguide PPLN (poling period of 17.0 μm and crystal length of 20 mm; HC Photonics) [23–26], and the photon state is given by

$$\frac{1}{\sqrt{2}}\left(|S\rangle_s|S\rangle_i + e^{i\phi_p}|L\rangle_s|L\rangle_i\right) \otimes \int d\omega^2 f(\omega_s,\omega_i)|\omega_s,\omega_i\rangle. \quad (1)$$

The subscripts s and i represent signal and idler photons that distribute to Alice and Bob. $|S\rangle_s|S\rangle_i$ denotes the state amplitude for the SPDC photon pair present in the earlier time bin whereas $|L\rangle_s|L\rangle_i$ denotes the state amplitude created in the latter time bin. The two state amplitudes are coherently superimposed with a relative phase ϕ_p, which then defines the time-bin entangled state. The relative phase term ϕ_p is fine-tuned to $\phi_p = 0$ to define a Bell state in the experiment. Simultaneously present with the time-bin state, the joint spectral amplitude $f(\omega_s,\omega_i)$ determines the spectral

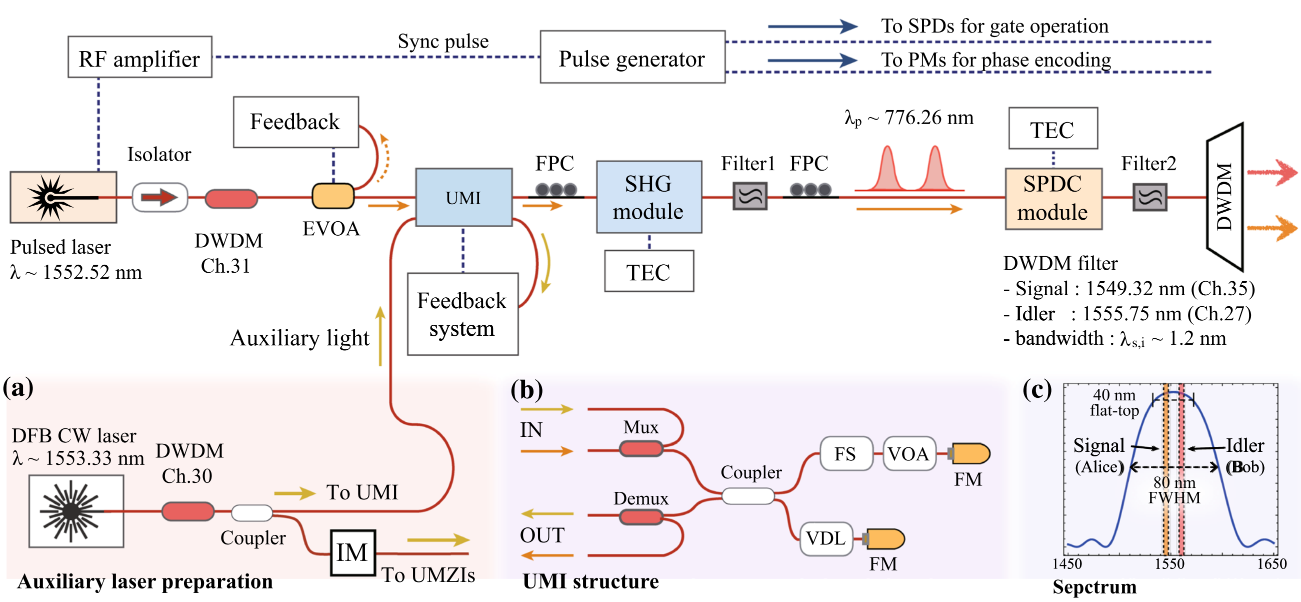

Fig. 2 Detailed setup for a source of time-bin entangled photons with an emphasis on the optical components and the supporting electronic systems. **a** an auxiliary CW laser implementation for feedback system, (**b**) the internal structure of the UMI, and (**c**) calculated marginal spectrum in SPDC photons. The channel numbers follow the ITU grid definitions. See the main text for details. *SPD* single-photon detector, *PM* phase modulator, *DWDM* dense wavelength-division multiplexing, *UMI* unbalanced Michelson interferometer, *VOA* variable optical attenuator, *EVOA* electronic VOA, *FPC* fiber polarization controller, *SHG* second harmonic generation, *SPDC* spontaneous parametric down-conversion, *TEC* thermo-electric cooler, *UMZI* unbalanced Mach-Zehnder interferometer, *IM* intensity modulator, *VDL* variable delay line, *FS* fiber stretcher, *FM* faraday mirror

correlation between the signal and the idler photons as well as the marginal spectral distribution of the individual SPDC photons. The down-converted photons are emitted symmetrically at a wavelength of 1552.52 nm and have a broad spectral bandwidth of up to 80 nm, covering the entire telecommunication C-band, as seen in Fig. 2c. Because the signal and the idler photons are highly anti-correlated due to energy-conservation, the time-bin entangled photon pairs can be, thus, selectively distributed to users with the desired correlated-channel pair through commercially available DWDM components coming from telecommunication technologies; here, the channel pair, Ch. 35 (λ_s=1549.32 nm) and Ch. 27 (λ_i=1555.75 nm), are selectively chosen for time-bin entanglement distribution.

The DWDMs in use have a 3-dB spectral bandwidth of 1.2 nm. The channel numbers follow the DWDM ITU grid specification. Residual pump radiations after the SPDC module are suppressed by Filter 2 which has an 80-dB rejection ratios and a 2.0-dB insertion losses. Filter 1 and Filter 2 in experiment are composed of in-series dichroic mirrors to reflect unwanted light; meanwhile, transmitted lights are coupled to a pigtailed fiber output. Prior to the SHG and the SPDC modules, fiber polarization controllers (FPCs) are installed and manually controlled for a proper polarization alignment to the optic axis of the PPLN crystals. For reliable operation, the PPLNs used in experiment are temperature-stabilized using TEC devices; PPLN:SHG and PPLN:SPDC are at 60.6°C and at 42.6°C, respectively.

The UMI in the experiment employs a common fiber-optic configuration in which telecom-band laser pulse is split at a fiber-optic coupler into two different arms, and each of those split pulses is reflected back toward the coupler via a pair of Faraday mirrors (FM). A temporal separation $\Delta\tau_p$ of 3.6 ns (or, equivalently, 72.0 cm of fiber) is given by different fiber lengths between two arms and is fine-adjusted with a variable delay line. For proper operation, the UMI comprises various fiber-based components, as shown in Fig. 2b; DWDM components for Mux/Demux, a fiber-optic 3-dB coupler, Faraday mirrors, a variable optical attenuator (VOA), a variable delay line (VDL; Advanced Fiber Resources, VDL-1550), and a piezo-actuated fiber stretcher (FS; General Photonics, FPS-002). The VOA prepares equally balanced time-bin modes. Note that a Michelson-type interferometer has two different paths inside and, thus, is subject to an unwanted phase drift. To resolve the phase drift issue, we introduced an auxiliary CW laser (Nortel networks, LC155CDC-20), shown in Fig. 2a, to actively stabilize the interferometer with a feedback system [32, 33]. In the following, we explain how to stabilize the Michelson interferometer; the unbalanced Mazh–Zehnder interferometers (UMZIs) for qubit analysis, as shown in Fig. 1, are also stabilized similarly.

The auxiliary laser operates at $\lambda \sim$ 1,553.33 nm (Ch. 30 ITU) and is stably manipulated using a laser diode controller (Thorlabs, LDC205) and a TEC controller (Thorlabs, TED200). After having being combined with the pulsed laser, the auxiliary light co-propagates the entire optical path of the UMI and undergoes the same thermal fluctuations as the pulsed laser, as shown in Fig. 2b. The coherence length of the auxiliary laser is sufficiently longer than the path length difference of the UMI to interfere with itself, and its interference signal is then exploited to feedback control the piezo-actuated fiber stretcher. Herein, the feedback system use the modulator bias controller (OZ Optics, MBC-DTS0170) to lock the interference signal at the desired phase (e.g., pump phase ϕ_p in Eq. (1)), the feedback signal of which is amplified up to 10 times and then sent to the fiber stretcher. The feedback system then phase-stabilizes the interferometer. The wavelength of the pulsed laser is located next to that of the auxiliary laser; thus, its spectrum tails are erased using DWDM components (Ch. 31 ITU) to isolate the feedback optical system. Note that the use of Faraday mirrors naturally auto-compensates for the polarization-mode

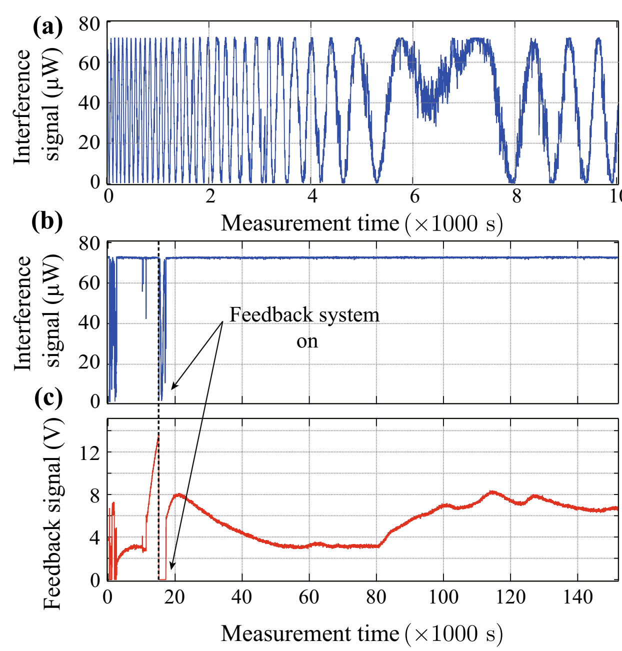

Fig. 3 Measurement results for a phase-stabilized interference signal in an unbalanced Michelson interferometer. Thermally affected interference signals are well depicted in (**a**) indicating that the interferometer does not stabilize even with time. When the feedback system starts to operate, the interference signal become constant, phase-locked, at a desired value (here, at the top fringe). The phase-locked interference signal can be seen in (**b**). However, corresponding feedback signal from modulator bias controller keeps changing to actively drive the pieozo-actuated fiber stretcher in (**c**). The feedback signal is ten times amplified and then sent to the fiber stretcher for feedback control

dispersion in the UMI, which enables stable feedback operation for a long time.

Whether or not the feedback system operates properly can be estimated by observing the interference signal from interferometer, and the measurement results are well described in Fig. 3. With feedback operation off, the interference signals fluctuate rapidly with time, the degree of which then slowly moderates as the interferometer module is protected from the thermally-unstable laboratory environment, as in Fig. 3a. However, the UMI needs to be much more stabilized for quantum communication. When the feedback system starts to operate, it shows a phase-locked interference signal after a few seconds of initialization, as in Fig. 3b, which represents the operation of a phase-stabilized interferometer. While the interference signal remains phase-locked and unchanged, the feedback-controlled drive signal from the bias controller continues to fluctuate with time due to the thermal phase drift, which is presented in Fig. 3c. The feedback system can stably continue to work day and night. The active feedback system in the Mach-Zehnder interferometers belonging to Alice and Bob in Fig. 1 is similarly operated.

In order to confirm the quantum correlations between signal and idler photons generated in a waveguide PPLN, we measured the coincidence counts (CC) and the accidental coincidence counts (ACC), as shown in Fig. 4a, by

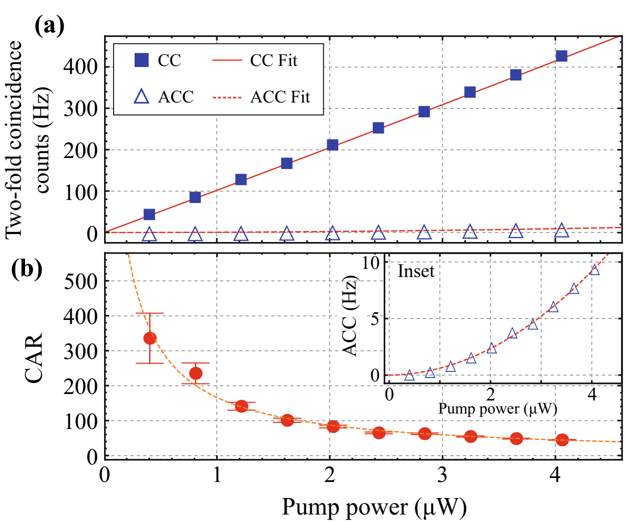

Fig. 4 Photon pair generation at a PPLN:SPDC crystal, i.e., (**a**) twofold coincidence and (**b**) coincidence-to-accidental count ratio (CAR), against average pump power. The coincidence counts (CC) and the accidental coincidence counts (ACC) are increasingly measured at higher pump power, but the ACC more steeply increases, as seen in the inset of (**b**) whereas CC increases linearly. Thus, the CAR measurement result, defined as $\frac{CC}{ACC}$, shows a gradual decrease with increasing pump power. The CAR value represents how much the photon detection includes uncorrelated noise in itself. The theoretical fits obtained from the analytical formulas in Eqs. (2) are drawn as red curves atop the experimental data. The error bars represent one standard deviation assuming Poissonian statistics

recording the twofold coincidence for photon pairs generated by identical and different pulses, respectively. Here, pulsed laser is not designed to go through the UMI, so time-bin modes are not defined for simplicity. The pump power is well-controlled using an electronic variable optical attenuator (EVOA; Thorlabs, V1550A) with a DAC-based feedback circuit (NI, USB-6008). The temporal correlation of the detection events for CC and ACC is measured by using a pair of InGaAs single-photon detectors (Aurea Technology, SPD-A-NIR) and analyzed by using a time-correlated single-photon-counting device (PicoQuant, Picoharp 300).

Analytically, the probability of coincidence and accidental coincidence can be formulated using experimentally-measured parameters [34]

$$\begin{aligned} P_{CC} &= \mu\eta_A\eta_B + (\mu\eta_A + d_A)(\mu\eta_B + d_B), \\ P_{ACC} &= (\mu\eta_A + d_A)(\mu\eta_B + d_B), \end{aligned} \tag{2}$$

where μ is the average number of photon pairs in a single pulse (which change with the pump power), η_A (η_B) is the overall detection efficiency (which includes fiber losses, insertion losses of the various optical components, like the SPDC module, Filter2, and DWDM components, e.g., and detector's quantum efficiency) measured by Alice (Bob), and d_A (d_B) is the detector's dark count probability for Alice (Bob).

The coincidence (P_{CC} in Eq. (2)) for the same pump pulse includes meaningful coincidence from the correlated photon pairs and also accidental coincidences (P_{ACC} in Eq. (2)) caused by uncorrelated photons from multiple pairs and the detector's dark counts. Such noise contribution, P_{ACC}, is generally unavoidable in an entanglement distribution due to the use of non-ideal detectors [34] and should be kept at the lowest level possible. The measurement results show that the coincidence counts are notably linearly proportional to the average pump power, i.e., increasing linearly from 41 to 424 Hz, implying that most of the coincidence events originate from the meaningful single-pair contribution of SPDC photons due to linear dependence of the SPDC photons on the mean pump power [35, 36]. Accidental coincidence contributions do exists, i.e, quadratically increasing from 0.12 to 9.45 Hz on average, but are clearly smaller, as seen in Fig. 4a. The measurement of individual photons shows a linearly increasing behavior of count rates with increasing pump power, ranging from 1400 Hz to 13 kHz for signal photons and 1500 Hz to 13.5 kHz for idler photons, and the two results are look alike due to their similar overall detection efficiencies.

To see how much the quantum correlation can be observed, we calculated the coincidence-to-accidental ratio (CAR) from the measured data, as shown in Fig. 4b; CAR is defined as $\frac{CC}{ACC}$. For sure, CAR $\gg 1$ can be found for correlated photon pairs and will increase as accidental coincidence noise is low, indicating a higher correlation between signal and idler photons. As the pump power increases, the CAR value gradually decreases due to the more rapid increase of accidental contributions from multiple photon-pair generations at a higher pump power, as seen in inset of Fig. 4b; the accidental coincidence counts are quadratically proportional to pump power. We achieve a high CAR value of more than 330 at a pump power of 0.4 μW, but only get ~40-Hz coincidence counts, and expect a higher CAR with decreasing pump power at the expense of obtainable count rates (with additional losses of DSF spools and interferometers, e.g., the coincidence will dramatically drop). We conduct all the experiments near at CAR $\sim$ 40, considering the tradeoff between entanglement quality and achievable counts. Note that the measured μ values with increasing pump power range from 0.002 pairs per pulse to 0.023 pairs per pulse and that the overall detection efficiency is approximately $\eta_{A,B} \sim 3.1\%$. The average number of SPDC photon pairs μ is estimated from the CAR data by using the relation $\mu \approx \frac{1}{\mathrm{CAR}-1}$ [34].

2.2 Time-bin entanglement analysis

In the time-bin entanglement measurement stage, each user (i.e., Alice and Bob) prepares his/her own unbalanced Mach-Zehnder interferometer in the Franson configuration [37], as shown in Fig. 1. The primary task of the interferometers is to encode rapidly the phases, i.e., ϕ_A and ϕ_B, to the incoming qubits (as seen in Eq. (1)). Figure 5 shows what kinds of fiber-optic components are organized in the UMZI and how they work on communication with various electronic systems. The UMZIs are made up of a pair of fiber optic couplers connected by optical fibers of different lengths with functional fiber-optic components between them. A fiber-optic phase modulator (PM; EOspace, PM-0S5-10-PFA-PFA-UL) lies in the short arm. The long arm, on the other hand, has an electronic fiber polarization controller (EPC; OZ Optics, EPC-400), a piezo-actuated fiber stretcher (FS; General Photonics, FPS-002), and a variable delay line (VDL; Advanced Fiber Resources, VDL-1550). In the following, the detailed operation of various electronic systems are explained.

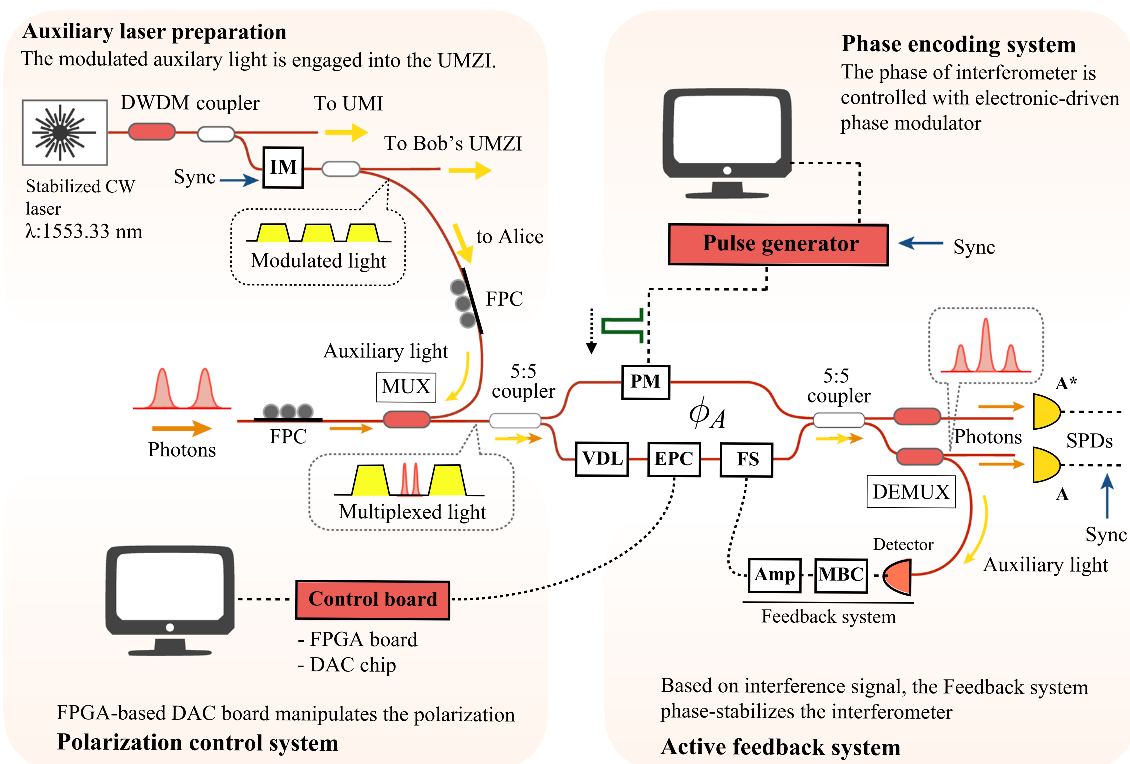

Fig. 5 Operation scheme for Alice's unbalanced Mach–Zehnder interferometer. The interferometer's main task is to fast encode the phase, i.e., ϕ_A, to the incoming time-bin qubits in all fiber-based implementation; the encoding phase of the interferometer is realized by using a high-speed phase modulator. For reliable operation, theUMZI should organize a more versatile device structure with supporting electronic systems, i.e., an active feedback and polarization control, to verify reliable time-bin encoding communication. The other user, Bob, has an identical interferometer. See the main texts for detailed explanations. *UMI* unbalanced Michelson interferometer, *UMZI* unbalanced Mach-Zehnder interferometer, *IM* intensity modulator, *FPC* fiber polarization controller, *PM* phase modulator, *VDL* variable delay line, *EPC* electronic polarization controller, *FS* fiber stretcher, *MBC* modulator bias controller, *Amp* amplifier, *FPGA* field-programmable gate array, *DAC* digital to analogue converter, *SPD* single-photon detector

If high-quality entanglement is to be ensured, the path-length difference of the UMZIs ($\Delta\tau_{A,B}$) needs to match that of the UMI (i.e., the temporal separation of $\Delta\tau_p \sim 3.6$ ns), and the photon polarizations in both arms must be the same. Note that, because the tolerance is only allowed within a bi-photon coherence length τ, i.e., $|\Delta\tau_A - \Delta\tau_B| \ll \tau$, an accurate length difference should be obtained using a variable delay line with a resolution of 30 μm. For a proper polarization alignment, the electric polarization controllers are exploited to make the photon's polarization in one arm identical to that in the other arm. A series of electrically-driven magnets are inside the EPC, and they induce a fiber-squeezed birefringence, i.e., polarization change, in accordance with the external drive voltage. We used an FPGA board (FPGA; NI, PCI-7813R) and a digital-to-analogue converter chip (DAC; MAXIM, AD5044BRUZ) to prepare a set of drive voltages (from - 5 V to +5 V), which enabled one to manipulate the photon's polarization automatically in a remote control.

Note that, because the UMZIs have two distinct paths inside, similarly to UMI, as seen in Fig. 5, the photons should suffer from thermally induced phase drift. The UMZIs are also actively stabilized by using an auxiliary laser of 1,553.33 nm to feedback control the piezo-actuated fiber stretcher. Unlike the UMI, however, the use of a fiber-optic phase modulator for qubit encoding might give an unnecessary phase to the interference signal of auxiliary CW light, which would preclude phase stabilization of the interferometers. To this end, we employed a fiber-optic intensity modulator (IM; iXblue, MXER-LN-10) to prepare intensity modulated auxiliary light of 30 ns in duration, the top region of which could still overlap enough to produce an interference signal without being disturbed by phase modulator's operation. Meanwhile, the time-bin photons and auxiliary light become temporally separated (see how auxiliary light and photons are multiplexed and demultiplexed in Fig. 5). More than a 25-dB high-extinction ratio is required for the auxiliary light to behave properly in the feedback system. The further process is similar to that in the UMI. The interference signal is used to feedback control the piezo-actuated fiber stretcher, which, in turn, phase-stabilizes the interferometer. Of note, is that the feedback system should use a low-bandwidth detector to alleviate the fast-modulated interference signal into averaged sums and that the averaged interference signal is used to feedback control the fiber stretcher. Indeed, the built-in detector for the modulator bias controller in use (MBC; OZ Optics, MBC-0020UB) has a low bandwidth of 2 kHz and is available in the feedback system. The wavelength of the auxiliary laser is located close to those of signal and idler photons; thus, the spectrum tails of the auxiliary light should be suppressed by using DWDM components (Ch. 30 ITU) to reduce the residuals in the signal/idler channels down to a zero-click level.

The time-bin qubits are measured by post-selecting the central peak through the detector's gated operation; the measurement bases for the time-bin qubits are set by choosing the phases of the Alice's and Bob's UMZIs (ϕ_A and ϕ_B) through a phase modulator and are correspondingly written as $\frac{1}{\sqrt{2}}\left(|S\rangle_A + e^{i\phi_A}|L\rangle_A\right)$ for Alice and $\frac{1}{\sqrt{2}}\left(|S\rangle_B + e^{i\phi_B}|L\rangle_B\right)$ for Bob. The used phase modulators feature a 10-GHz bandwidth of high-speed operation and a 3.5-V low half-wave voltages. The time-bin photons are detected using a pair of InGaAs single photon detectors belonging to Alice and Bob (Aurea Technology, SPD-A-NIR). The detectors, operated in the triggered mode synchronized to the repetition rate of the pulsed laser, feature a quantum efficiency of 20% with a dead time of 10 μs. The detection window is set to 1.5 ns to suppress possible noise clicks, and the dark counts are measured to be around $d_A \approx d_B \approx 8 \times 10^{-6}$ counts per detection window. The temporal correlation of the detection events is measured by using a time-correlated single-photon-counting device (UQDevices, Logic16). The overall detection efficiency $\eta_{A(B)}$ (which includes fiber losses, insertion losses of the various optical components like SPDC module, Filter2, DWDM components, e.g., and detector's quantum efficiency), measured by Alice (Bob), is typically ~ 1.3%. In the experiment, the two users are connected each via dispersion-shifted fiber spools (FSC-DSF-spool; Lucent); therefore, time-bin entanglement is established between Alice and Bob via 60-km-long optical fibers. The overall detection efficiencies $\eta_{A,B}$ is decreased to typically $\sim 0.3\%$ due to fiber transmission loss (~ 0.2 dB/km). Compared with a standard single-mode optical fiber, the used DSFs are designed to have a zero-dispersion wavelength near 1550 nm so that dispersion-originated pulse broadening can be kept to a minimum during fiber transmission. Therefore, reliable distribution of time-bin entanglement could be realized without possibly temporal overlapping two time-bin modes even at a long-range distribution.

3 Results and discussions

3.1 Analysis of the system performance

Here, we analytically characterize the system performance with special emphasis on long-lasting system stability. To begin with, a way of quantifying the system performance is presented in terms of experimentally measurable parameters. The associated data are two-photon interference fringes that oscillate as a function of the sum of the phases in Alice's and Bob's UMZIs. Then, we deduce the entanglement quality by measuring the two-photon visibilities V from the data, implying a figure of merit for the QC system performance [23–27]. For the quantum correlation, the condition of violating the CHSH inequality is well known to be $V > 0.707$ [38].

For the time-bin entangled photon state in Eq. (1) with $\phi_p = 0$, i.e., $\frac{1}{\sqrt{2}}\left(|S\rangle_s|S\rangle_i + |L\rangle_s|L\rangle_i\right)$, the two-fold coincidence probability $P_{A,B}$ between the detectors at Alice's and Bob's locations, in an ideal setup, can be written as

$$P_{A,B} = \frac{1}{4} + \frac{1}{4}\cos(\phi_A + \phi_B), \tag{3}$$

where the subscripts are as shown in Fig. 1. The other coincidence probabilities between other pairs of detectors are similarly presented. The ideal system will, as shown in Eq. (3), will produce a unity of the two-photon visibility and therefore allow for a perfect quantum communication.

Apart from the ideal setup, however, the performance of the overall QC system is restricted due to suboptimal situations (e.g., the quality of interferometers, non-ideal single photon-pair source, the noisy channel, and the detectors with dark counts), which is, therefore, required to analyze quantitatively. Slightly modified from Eq. (3), the derived formula for the probability of a two-fold coincidence event $P^*_{A,B,}$ reads [34]

$$\begin{aligned} P^*_{A,B} =& \frac{1}{8}\mu\eta_A\eta_B\left(\frac{1}{2} + \frac{1}{2}V_0\cos(\phi_A + \phi_B)\right) \\ &+ \frac{1}{16}\mu^2\eta_A\eta_B + \frac{1}{4}\mu\eta_A d_B + \frac{1}{4}\mu\eta_B d_A + d_A d_B, \end{aligned} \tag{4}$$

where μ is the average number of photon pairs, η_A (η_B) is the overall detection efficiency (which includes all the transmission losses until detection) measured by Alice (Bob), V_0 is the maximum achievable visibility (limited by the interferometer quality), $\phi_A(\phi_B)$ is the encoding phase of Alice's (Bob's) UMZI, and d_A (d_B) is dark count probability of the Alice's (Bob's) detector. Here, note that the average number of time-bin entangled paired photons μ is defined as the average number per two temporal modes (i.e., a single time-bin qubit). The first term in Eq. (4) refers to the contribution by the entangled photon pair while the second term represents accidental contributions caused by uncorrelated photons from multiple pairs and the detector's dark counts. Notably, the accidental coincidence term (together with V_0) degrades the quality of the two-photon interference measurement, which can be observed analytically in two-photon interference visibility V below:

$$\begin{aligned} V &= \frac{\frac{1}{8}\mu\eta_A\eta_B}{\frac{1}{8}\mu\eta_A\eta_B + \frac{1}{8}\mu^2\eta_A\eta_B + \frac{1}{2}\mu\eta_A d_B + \frac{1}{2}\mu\eta_B d_A + 2d_A d_B}V_0 \\ &\approx \frac{1}{1+\mu}V_0, \end{aligned} \tag{5}$$

where the approximation of 2nd line assumes the limiting situation; i.e., $\frac{1}{4}\mu\eta_{A(B)} \gg d_{A(B)}$, the contribution of dark counts is significantly smaller than that of an entangled photon pair. But this approximation is usually reasonable in the given experimental conditions; a typical value of detection efficiency $\eta_{A,B}$ $\sim 1\%$ (with no spools), average pair number $\mu > 0.01$, and detectors operating in narrow gate window of 1.5 ns, thus giving a small dark count probability of $\sim 8 \times 10^{-6}$ per gate window. The approximated form of Eq. (5) then implies a simple dependence of the visibility solely on the μ value and, thus, gives an insight of how the QC system optimizes.

We experimentally investigate changes in the two-photon visibility V over a wide range of pump powers corresponding to μ ranging from 0.02 to 0.10. One might want to increase μ to get higher generation rates of entangled photon pairs. However, this comes at the cost of increased multi-pair event contributions, ultimately reducing the observed two-photon visibility, as seen in Fig. 6. The linear decrease in two-photon visibility with increasing μ is observed in accordance with Eq. (5), $V \approx \frac{1}{1+\mu}V_0$. On the contrary, if the pump power is too low, the visibility is also significantly reduced as the contribution of the entangled pair coincidence event drops below the noise contributions in the detection system; however, this is not observed in the experiment due to the use of a low dark count noise condition, i.e., $\frac{1}{4}\mu\eta_{A(B)} \gg d_{A(B)}$. As extrapolated to $\mu \to 0$ instead, the visibility data seem to gradually increase and then approach V_0 asymptotically (i.e., $\lim_{\mu\to 0}\frac{1}{\mu+1}V_0 = V_0$), which enables us to get a maximum achievable visibility. This V_0 value represents how much the interferometers, UMI and the UMZIs, belonging to Alice

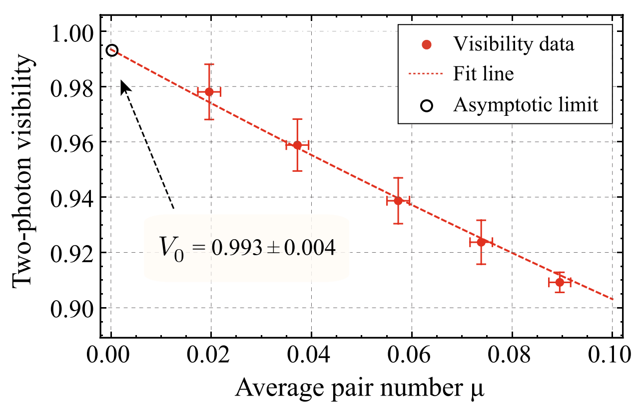

Fig. 6 Two-photon visibility results as a function of the average number of photon pairs μ. A gradual increase in the two-photon interference visibility with decreasing μ is observed due to the lower generation of multiple SPDC photon pairs in accordance with Eq. (5), $V \approx \frac{1}{1+\mu}V_0$; the data fit line (red dashed line) is extrapolated to a high value $V_0 \sim 0.993$, implying a maximum achievable visibility (limited by quality of implemented system). The visibility results also give an impressive hint to optimizing the overall system by modifying μ to ensure high performance in quantum communication; in the experiment, $\mu \sim 0.055$ is chosen. The DSF spools are not connected to emphasize the system implementation itself

and Bob, are ideally prepared; such degradation factors include mismatches in the polarization modes and the state amplitudes between the two arms in the interferometer. In the experiment, we were able to get an exceptionally high value $V_0 \sim 0.991$ from the data, thus implying that the high-quality interferometers were prepared sufficiently to realize a time-bin entanglement quantum communication through our fiber-optically implemented system. Also, we used a μ value of 0.055, which, in turn, led to a typical visibility of $V \sim 0.94$ and to a typical two-fold coincidence rate of ~ 22.0 Hz. Note that the expected result well exceed the threshold of 0.707 for violation of the CHSH inequality, and this choice is a trade off between system performance and communication rates. The μ value can be estimated from the CAR data by using the formula $\mu \approx \frac{2}{\mathrm{CAR}-1}$ [34].

Reliable operation of the overall QC system is verified by measuring the two-fold coincidence of time-bin entangled photons for a long time. The experimental results for a 48-hour operation are shown in Fig. 7: without DSF spools in (a) and with DSF spools in (b). Given the prepared time-bin Bell state, i.e., $\frac{1}{\sqrt{2}}(|S\rangle_s|S\rangle_i + |L\rangle_s|L\rangle_i)$, we collect coincidence counts over 48 hours of measurement under nominal conditions (sampling period of 60s and 300s, respectively); meanwhile, phase ϕ_B is discretely changed every 12 h, $\phi_B = 0, \pi/3, 2\pi/3$, and π, successively while phase ϕ_A is fixed at $\phi_A = 0$. Note that, both *w* and *w/o* spools, the constant twofold coincidence counts of

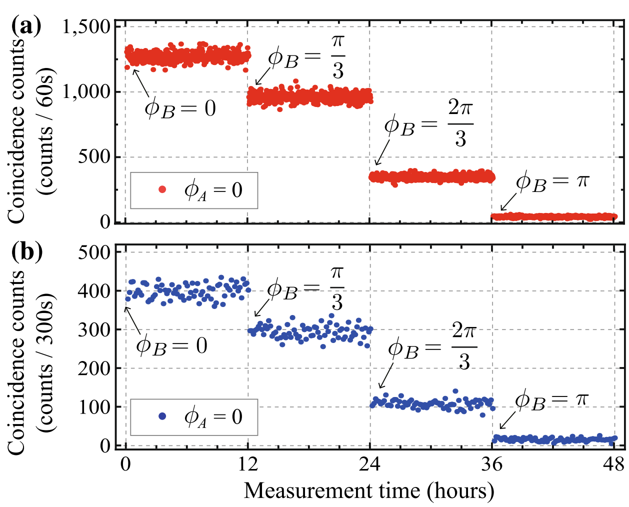

Fig. 7 Long-term stability test of time-bin two-photon measurement, represented by the measurement data of two-fold coincidence counts for 48 h: (**a**) w/o and (**b**) with DSF spools. Every 12 hours, the phase ϕ_B is discretely increased while the phase $\phi_A = 0$ is constant. Encoded phases ϕ_B are displayed in (**a**) and (**b**), and a gradual decrease in the coincidence counts is observed in accordance with Eq. (3), i.e., $P_{A,B} = \frac{1}{2} + \frac{1}{2}\cos(\phi_A + \phi_B)$. Each data point in (**a**) and (**b**) accumulates for 60 s and 300 s, respectively, to suppress statistical errors

time-bin photons are, within the statistical tolerance, measured reliably over the measurement time, and the step changes are well observed as a function of the phases' sum, i.e., $\phi_A + \phi_B$; whereas single counts of both signal and idler photons are constantly measured at rates up to $\sim 3.4 \times 10^3$ Hz without spools and $\sim 9.0 \times 10^2$ Hz with spools for all measurement times. The results indicate that the overall setup is well stabilized; reliable distribution of time-bin entangled photons is available even in a long time through the help of the commercially available electronic systems, as discussed in previous section.

3.2 Time-bin entanglement distribution

We now study how well the time-bin entanglement can be established between communicating users in our QC system. The two users, i.e., Alice and Bob, are connected over a 60-km-long standard fiber link made of two 30-km-long DSF spools and thereby simulating a realistic implementation of an existing fiber quantum channel. The quality of time-bin entanglement is quantified by observing two-photon correlations: the interference visibility V [23–27] or the violation of the CHSH inequality [38]. In the experiment, the two-photon visibility V can be obtained through numerical fits to the given data, and CHSH S parameters are obtainable with proper phases settings [38]. The corresponding results are shown in Fig. 8.

First of all, we measured the two-photon correlations without DSF spools. Here, the entanglement source is engineered at the average number of photon pairs μ to choose a fair compromise between coincidence rate and entanglement quality for a QC scenario. For the particular trade-off, we pick $\mu \sim 0.055$, for which we expect $V \sim 0.94$, as can seen in Fig. 6, and the corresponding measurements on time-bin entangled photons could yield the two-photon visibilities $V = 0.940 \pm 0.003$, and at least a 6σ violation of the CHSH inequality (i.e., $S = 2.654 \pm 0.101$). Then, with DSF spools installed, the users are fiber-optically linked at separation of up to 60 km. Due to the fiber loss (~ 0.2 dB/km), the twofold coincidence rates of around 22.0 Hz decreased down to 1.3 Hz whereas the visibility of the two-photon interference and the CHSH S parameter, however, are not altered significantly. In the experiment, we observe $V = 0.923 \pm 0.007$ and 4σ violation of the CHSH inequality (i.e., $S = 2.574 \pm 0.131$), demonstrating the excellent establishment of time-bin entanglement between users and the high quality of the QC system (including the entanglement source and the associated measurement setup). Note that all visibility measurement results well exceed the threshold of 0.707, even with DSF spools, which is required to violate the CHSH inequality, and the actual measurements of CHSH S parameters are well above the threshold of $S = 2$ [38]. In

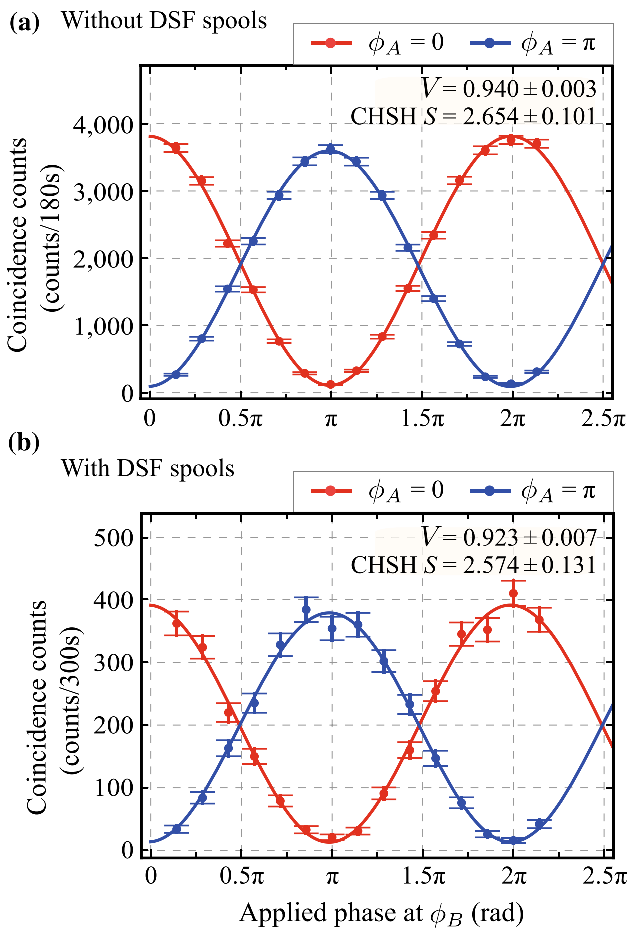

Fig. 8 Experimental results of two-photon correlation measurements due to time-bin entangled photons. The blue (red)-colored data represent the exemplary interference fringes in measuring the signal photon at local phase $\phi_A = \pi$ ($\phi_A = 0$), and the colored lines are numerical fits to each data set. The interference data are measured (**a**) w/o DSF spools and (**b**) with DSF spools. The 30-km optical fiber spools are connected to Alice and Bob, which implements the total 60-km quantum channel between the two users. Thus, the long-distance channel reduces the coincidence rate due to fiber attenuation ($\sim$ 0.2 dB/km), but hardly degrades the two-photon visibilities and the CHSH S parameters, the experimental values of which are displayed in each plot. The error bars represent one standard deviation assuming Poissonian statistics

addition, our visibility results also satisfy $V > 0.78$ condition, which is necessary for a successful key generation; an entanglement-based QKD protocol requires less than an 11% quantum bit error rate (QBER) [39, 40], i.e., $V > 0.78$ [41].

4 Conclusion

Here, we report a quantum communication system intended to be compliant with the Ekert91 protocol [1] in Franson configuration [37], e.g., capable of distributing time-bin entangled photons reliably over 60-km-long fiber channels. The use of time-bin entangled qubits in quantum communication features outstanding robustness for transmission in optic fiber channels and, thus, shows a potential for enabling long-range quantum operation. However, the time-bin modes are also susceptible to thermally induced degradation, especially in fiber-based environments, and should rely on very stable interferometers. In particular, the introduction of an active phase-stabilization system with a frequency-stabilized auxiliary laser and feedback loop electronics allows long-term stability over more than a day and a night, which is a sufficiently long time for quantum communication to be achieved. Given the extremely-stable QC system, we demonstrated that time-bin entangled photons can be reliably distributed to distant users in all fiber-based implementation and that high-quality of their entanglement required in quantum communication is proven by showing a high value of the two-photon interference visibility $V \sim 0.923$ and violation of the CHSH Bell inequality by more than 4σ.

Further, our study, carried out on the entanglement distribution over DWDM channels, gives the potential to achieve a higher communication rate between users with a broadband photon source. Users perform a local multiplexing strategy to obtain a rate increase equal to the number of multiplexed pairs of wavelength-correlated channels; indeed, they are distinguishable from each other via slightly modified temporal delays. We remark that the SPDC photon pairs have roughly 40 nm of flat-top spectral bandwidth, implying that roughly 25 channel pairs can be exploited to improve our QC system's performance, i.e., the communication rate can be added up to a 25-fold increased rate without modifying the entangled photon source and, more importantly, without sacrificing the distributed entanglement quality in the fiber-optic links. Therefore, our experimental demonstration proves the importance of our study in long-range entanglement-based quantum communication and further paves the way toward the future quantum network.

Funding This work was supported in part by the National Research Foundation of Korea (Grant No. 2019R1A2C3004812), the affiliated institute of ETRI (Grant No. 2019-110), and the ITRC support program (IITP-2021-2020-0-01606).

Availability of data and materials The data that support the plots within this paper and other findings of this study are available from the corresponding author upon reasonable request.

Declarations

Conflict of interest The authors declare no competing interests.

References

1. A.K. Ekert, Quantum cryptography based on Bell's theorem. Phys. Rev. Lett. **67**(6), 661–663 (1991)
2. R. Ursin et al., Entanglement-based quantum communication over 144 km. Nat. Phys. **3**(7), 481–486 (2007)
3. J. Yin et al., Entanglement-based secure quantum cryptography over 1,120 kilometres. Nature **582**(7813), 501–505 (2020)
4. C.H. Bennett, G. Brassard, C. Crépeau, R. Jozsa, A. Peres, W.K. Wootters, Teleporting an unknown quantum state via dual classical and Einstein-Podolsky-Rosen channels. Phys. Rev. Lett. **70**(13), 1895–1899 (1993)
5. D. Bouwmeester, J.-W. Pan, K. Mattle, M. Eibl, H. Weinfurter, A. Zeilinger, Experimental quantum teleportation. Nature **390**(6660), 575–579 (1997)
6. D. Boschi, S. Branca, F. De Martini, L. Hardy, S. Popescu, Experimental Realization of Teleporting an Unknown Pure Quantum State via Dual Classical and Einstein-Podolsky-Rosen Channels. Phys. Rev. Lett. **80**(6), 1121–1125 (1998)
7. Y.-H. Kim, S.P. Kulik, Y. Shih, Quantum Teleportation of a Polarization State with a Complete Bell State Measurement. Phys. Rev. Lett. **86**(7), 1370–1373 (2001)
8. M. Hillery, V. Bužek, A. Berthiaume, Quantum secret sharing. Phys. Rev. A **59**(3), 1829 (1999)
9. W. Tittel, H. Zbinden, N. Gisin, Experimental demonstration of quantum secret sharing. Phys. Rev. A **63**(4), 042301 (2001)
10. S. Gaertner, C. Kurtsiefer, M. Bourennane, H. Weinfurter, Experimental Demonstration of Four-Party Quantum Secret Sharing. Phys. Rev. Lett. **98**(2), 020503 (2007)
11. A. Mair, A. Vaziri, G. Weihs, A. Zeilinger, Entanglement of the orbital angular momentum states of photons. Nature **412**(6844), 313–316 (2001)
12. A.C. Dada, J. Leach, G.S. Buller, M.J. Padgett, E. Andersson, Experimental high-dimensional two-photon entanglement and violations of generalized Bell inequalities. Nat. Phys. **7**(9), 677–680 (2011)
13. J.-C. Lee, K.-K. Park, T.-M. Zhao, Y.-H. Kim, Einstein-Podolsky-Rosen Entanglement of Narrow-Band Photons from Cold Atoms. Phys. Rev. Lett. **117**(25), 250501 (2016)
14. M. Erhard, M. Krenn, A. Zeilinger, Advances in high-dimensional quantum entanglement. Nat. Rev. Phys. **2**(7), 365–381 (2020)
15. H.J. Kimble, The quantum internet. Nature **453**(3), 1023–1030 (2008)
16. S. Wehner, E. David, H. Ronald, Quantum internet: a vision for the road ahead. Science **362**, 6412 (2018)
17. J. Trapateau, J. Ghalbouni, A. Orieux, E. Diamanti, I. Zaquine, Multi-user distribution of polarization entangled photon pairs. J. Appl. Phys. **118**(14), 143106 (2015)
18. Y.-H. Li, Z.-Y. Zhou, Z.-H. Xu, L.-X. Xu, B.-S. Shi, G.-C. Guo, Multiplexed entangled photon-pair sources for all-fiber quantum networks. Phys. Rev. A **94**(4), 043810 (2016)
19. T. Ikuta, H. Takesue, Four-dimensional entanglement distribution over 100 km. Sci. Rep. **8**(1), 1–7 (2018)
20. S. Wengerowsky, S.K. Joshi, F. Steinlechner, H. Húbel, R. Ursin, An entanglement-based wavelength-multiplexed quantum communication network. Nature **564**(7735), 225–258 (2018)
21. S. Wengerowsky et al., Entanglement Distribution over a 96-km-Long Submarine Optical Fiber. Proc. Natl. Acad. Sci. U.S.A. **116**(14), 6684–6688 (2019)
22. S.K. Joshi, D. Aktas, S. Wengerowsky, M. Lončarić, S.P. Neumann, B. Liu, T. Scheidl, G.C. Lorenzo, Ž Samec, L. Kling et al., A trusted node-free eight-user metropolitan quantum communication network. Sci. Adv. **6**(36), eaba0959 (2020)
23. I. Marcikic, H. de Riedmatten, W. Tittel, V. Scarani, H. Zbinden, N. Gisin, Time-bin entangled qubits for quantum communication created by femtosecond pulses. Phys. Rev. A **66**(6), 062308 (2002)
24. I. Marcikic, H. de Riedmatten, W. Tittel, H. Zbinden, M. Legré, N. Gisin, Distribution of Time-Bin Entangled Qubits over 50 km of Optical Fiber. Phys. Rev. Lett. **93**(18), 180502 (2004)
25. J.M. Donohue, M. Agnew, J. Lavoie, K.J. Resch, Coherent Ultrafast Measurement of Time-Bin Encoded Photons. Phys. Rev. Lett. **111**(15), 153602 (2013)
26. O. Kwon, K.-K. Park, Y.-S. Ra, Y.-S. Kim, Y.-H. Kim, Time-bin entangled photon pairs from spontaneous parametric down-conversion pumped by a cw multi-mode diode laser. Opt. Express **21**(21), 25492–25500 (2013)
27. D. Aktas, B. Fedrici, F. Kaiser, T. Lunghi, L. Labonté, S. Tanzilli, Entanglement distribution over 150 km in wavelength division multiplexed channels for quantum cryptography. Laser&Photonics Reviews **10**(3), 451–457 (2016)
28. H. Zbinden, J. Brendel, N. Gisin, W. Tittel, Experimental test of nonlocal quantum correlation in relativistic configurations. Phys. Rev. A **63**(21), 022111 (2001)
29. T. Inagaki, N. Matsuda, O. Tadanaga, M. Asobe, H. Takesue, Entanglement distribution over 300 km of fiber. Opt. Express **21**(20), 23241–23249 (2013)
30. T. Honjo, S.W. Nam, H. Takesue, Q. Zhang, H. Kamada, Y. Nishida, O. Tadanaga, M. Asobe, B. Baek, R. Hadfield, S. Miki, M. Fujiwara, M. Sasaki, Z. Wang, K. Inoue, Y. Yamamoto, Long-distance entanglement-based quantum key distribution over optical fiber. Opt. Express **16**, 19118 (2008)
31. H. Takesue, K.-I. Harada, K. Tamaki, H. Fukuda, T. Tsuchizawa, T. Watanabe, K. Yamada, S.-I. Itabashi, Long-distance entanglement-based quantum key distribution experiment using practical detectors. Opt. Express **18**, 16777 (2010)
32. P. Toliver, J.M. Dailey, A. Agarwal, N.A. Peters, Continuously active interferometer stabilization and control for time-bin entanglement distribution. Opt. Express **23**(4), 4135–4143 (2015)
33. S.-B. Cho, H. Kim, Active stabilization of a fiber-optic two-photon interferometer using continuous optical length control. Opt. Express **24**(10), 10980–10986 (2016)
34. H. Takesue, K. Shimizu, Effects of multiple pairs on visibility measurements of entangled photons generated by spontaneous parametric processes. Opt. Commun. **283**(2), 276–287 (2010)
35. C. K. Hong, L. Mandel, Theory of parametric frequency down conversion of light, Phys. Rev. A **31**(4) 2409-2418
36. Z. Y. Ou, X. Y. Zou, L.J. Wang, L. Mandel, Experiment on non-classical fourth-order interference, Phys. Rev. A **42**(5), 2957-2965
37. J.D. Franson, Bell inequality for position and time. Phys. Rev. Lett. **62**, 2205 (1989)
38. J.F. Clauser, M.A. Horne, A. Shimony, R.A. Holt, Proposed experiment to test local hidden-variable theories. Phys. Rev. Lett. **23**(15), 880–884 (1969)
39. M. Koashi, J. Preskill, Secure quantum key distribution with an uncharacterized source. Phys. Rev. Lett. **90**(5), 057902 (2003)
40. X. Ma, C.-H.F. Fung, H.-K. Lo, Quantum key distribution with entangled photon sources. Phys. Rev. A **76**(1), 012307 (2007)
41. N. Gisin, G. Ribordy, W. Tittel, H. Zbinden, Quantum cryptography. Rev. Mod. Phys. **74**(1), 145 (2002)